12

2D Simulation of Normal Penetration Using the Unified Strength Theory

12.1 Introduction

A great deal of researches have been conducted on impact and penetration problems. The penetration studies include various experimental, analytical and computational simulations. "Projectile penetration into a semi-infinite target" by an analytical method using the unified strength theory has been described in (Yu et al., 2009). These studies were done by Li JC (2002), Wei XY (2003) and Wang YB (2004) at Xi'an Jiaotong University, Xi'an China. Systematical results can be obtained by using the unified strength theory. The computational simulation of penetration with Yu's UST (Unified Strength Theory) and AutoDYN for 2D normal penetration, penetration of concrete slabs using UST and SPH (Smoothed Particle Hydrodynamics) methods will be discussed in this chapter. The 3D penetration and perforation will be studied in the next chapter.

In a purpose-built protective building structure, a concrete slab and wall may be required to withstand the effects of missile impact. The impact may be due to a variety of missiles that differ in shape, size and cruising velocity, such as bullets, fragments, tornado-generated missiles, accident generated missiles, etc. Based on the relative deformability between a missile and a target, a missile may be regarded as either a "hard" or "soft" one. For a hard missile, its deformation is considerably smaller than the deformation of the target. Very often, it is regarded as a rigid and non-deformable body. To predict the extent of penetration and/or perforation, there is a wealth of empirical and semi-empirical formulae available. On the other hand, a soft missile deforms considerably compared to the

---

This chapter was contributed by Professors Zhou XQ, Qiang HF, Xi'an High Technological Institute, Xi'an, China and Professor Fan SC, Nanyang Technological University, Singapore

M.-H. Yu et al., *Computational Plasticity*

deformation of the target. The responses of the missile and target are coupled. This renders the prediction more difficult. However, some approximate decoupling methods are available. These methods express the influence of the projectile's deformation as a reduction factor. Most of the empirical methods used in penetration and perforation prediction are solely based on a statistical fit of experimental data.

Nowadays, the investigation of highly dynamic events such as missile impacts and loading by blast waves is supported by numerical calculation. Wave propagation codes or "hydrocodes" have become a valuable tool for analyzing the propagation of stress waves in fluids and solids (Riedel et al., 1999). In general, these hydrocodes are based on well established continuum mechanics principles. The principal advantages of hydrocodes are that they can tackle a wide variety of impact problems, provide detailed information and cope with large displacement. A discrete element model is also used to predict the penetration depth and the perforation caused by a non-deformable missile against a thin reinforced concrete slab (Shui et al., 2009).

In the simulation, the material model plays a vital role. To achieve the accuracy it should be able to capture all major characteristics. On the other hand, a robust numerical procedure should be in place to guarantee the validity and the numerical stability. The Unified Strength Theory (UST) is adopted in defining the material strength effects and constructs dynamic multifold limit/failure surfaces including an elastic limit surface, failure surface and residual failure surface. The proposed model is incorporated into the AutoDYN hydrocode via the user defined subroutine function. The Smooth Particle Hydrodynamics (SPH) procedure seems to offer great promise in making such simulations more practical.

In this chapter, the numerical simulation of concrete against penetration will be described. The UST is implemented into AutoDYN and numerical examples of the penetration of concrete slabs are given. This work was conducted by Dr. Zhou Qiaoqing and Dr. Qiang HF under the supervision of Professor Fan SC at Nanyang Technological University, Singapore. The unified strength theory with parameter b=0.6 is used for simulation of penetration.

A two-dimensional axisymmetric numerical simulation for the projectile-and-target model under high speed impact is also carried out using the Smooth Particle Hydrodynamics (SPH) procedure in this chapter. In the simulation, the available hydrocode AutoDYN is employed with two key enhancements for material modeling. Firstly, an empirical nonlinear equation of state is employed for concrete material. Secondly, the unified strength theory (UST, Yu, 1991; 1992) is adopted in defining the material strength effects, and dynamic multifold limit/failure surfaces including elastic limit surface, failure surface and residual failure surface are constructed. These two enhancements are incorporated into the AutoDYN hydrocode via the user defined subroutine function by Professors Fan and Qiang at Nanyang Technological University, Singapore (Fan and Qiang, 2001; Qiang and Fan, 2002). The results obtained from the numerical simulation are compared with available experimental data. Good agreement is observed. It demonstrates that the proposed model can be used to predict not only the damaged

areas and reduction in velocity of the projectile during the perforation process, but also the debris clouds from the spalling process.

The objectives of this study are:

(1) To develop a new static multi-surface strength material model for static modeling of concrete based on Yu's unified strength theory (Yu's UST).

(2) To calculate some numerical examples on static analysis of a concrete member, and compare the numerical results with the test results.

(3) To develop a dynamic material model for concrete penetration analysis based on Yu's UST and incorporate the developed model into the AutoDYN (2000) through its user's subroutine function.

(4) To simulate the 2D and 3D perforation process of a reinforced concrete slab impacted by a steel projectile.

(5) The 3D simulation of the perforation process and oblique penetration will be described in the next chapter.

12.2 Penetration and Perforation

The physical phenomena associated with a projectile penetrating/perforating a concrete target are very complicated. The nature of the deformations taking place in both the projectile and the target during the penetration process need to be understood. This involves the material properties of both the projectile and the target. It also depends on the impact velocities and the nose shape of the projectile. In the penetration process, the stress waves initiated by the impact play an important role. The subsequent propagation of the stress waves creates a series of events including spalling, scabbing and fracture of the target.

When a projectile hits a target, three types of response can occur. Firstly, the projectile can ricochet, i.e. the projectile rebounds from the impacted surface or it skims the impacted surface with a reduced velocity. Secondly, the projectile can penetrate into the target without completing its passage through the body. Thirdly, perforation can occur when the projectile has sufficient energy to penetrate through the target. Very often, perforation of the target (especially for relatively thin targets) can occur even at an impact velocity well below that required to achieve complete penetration. It is probably due to the scabbing effect, which reduces the effective thickness of the target.

The processes of penetration and perforation of concrete are summarized in Fig. 12.1. Once the initial projectile velocity is large enough to damage the concrete, pieces of its spall from the impact face of the target form a crater, which extends over a considerably greater area than the impact area. As the impact velocity increases, the projectile penetrates deeper and it produces a hole in the concrete with a diameter only slightly greater than that of the projectile diameter. A further increase in the initial projectile velocity results in cracking and then scabbing (ejection) of concrete from the rear surface. The zone of scabbing is generally more extensive but less deep than that of the front spall crater. Since the

ejected concrete pieces (from the rear surface) could themselves constitute a hazard, it is often necessary to define two thicknesses when designing a protective shield: the minimum thickness to prevent perforation and the minimum thickness to prevent scabbing. The Sandia crash test for penetration and perforation of a concrete slab (Zhou, 2002; 2007) is shown in Fig. 12.2.

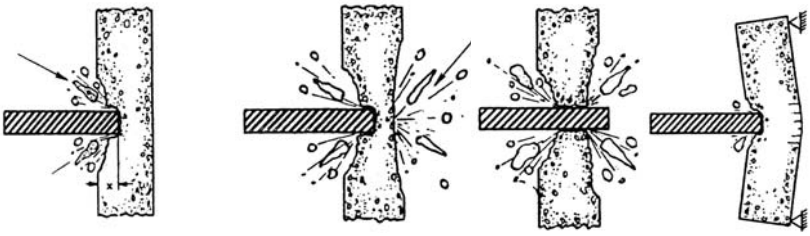

(a) Missile penetration and spalling (b) Target scabbing (c) Penetration (d) Overall target response

Fig. 12.1 Penetration and perforation of concrete slabs by non-deforming projectiles (Kennedy, 1976)

Fig. 12.2 A test for penetration and perforation of concrete slab (Sandia crash test)

Plain concrete is generally strong in compression and relatively weak in tension. Therefore, the compressive wave generated in the target does not cause much damage to the target. The failure due to impact is governed by the dynamic tensile strength of the concrete. Spalling occurs at the periphery of the impact area where maximum tensile stress exits (due to the surface stress wave). On the other hand, scabbing is caused by the tensile waves, resulting from the reflection of compressive waves at the free surface. When the compression pulse reaches the rear face of the target, it is reflected as a tensile wave. (This is necessary because the sum of the stresses due to the incident and the reflected waves must vanish at the free surface.) The tensile wave travels back into the target and away from the

rear face. Since the concrete material cannot withstand such large tension, scabbing occurs close to the rear free boundary (Laible, 1980).

The dynamic failure mechanism of concrete is intricate since discontinuities such as cleavage cracks and defects with different shapes and orientations are commonly encountered in concrete and they have significant influence on the deformation and failure characteristics of concrete (Herrmarm, 1969). The initially existing cracks and defects will be nucleated, and will evolve until the material loses strength, when subjected to dynamic loading. The damaged theory has been considered to be more suitable for the cleavage analysis of the concrete material.

How to define the failure criterion of the targets is critical for better analyzing penetration problems (Jonas and Zukas, 1978). The failure criteria such as the Mohr-Coulomb strength theory, the Huber-von Mises criterion and the Tresca yield criterion were often applied to penetration problems, as can be seen from the literature. These criteria do not completely consider all of the stress components in the stress space. The effect of intermediate principal stress is not taken into account in the Tresca criterion and the Mohr-Coulomb strength theory, which are not consistent with the test results of many materials. A unified strength theory, which was suggested by Yu (1991; 1992), considers all of the components in the stress space. It covers a series of strength theories, such as the Mohr-Coulomb's single-shear strength theory and the twin-shear strength theory (Yu, 1985) when the tension and compression strengths of materials are different, as well as the Tresca criterion, the Huber-von Mises criterion and the twin-shear criterion when the tension and compression strengths of materials are identical.

In this research, the unified strength theory is applied to modeling penetration and a unified plasticity-damage penetration model related to the crack density is proposed by Zhou (2002) and Fan-Qiang (2001). The relationship between radial traction and velocity at the cavity-surface can be obtained by analyzing the distributions of stress and velocity of the target material. Based on the cylindrical cavity expansion theory and spatial axisymmetrical unified characteristics line theory (Yu et al., 2001), the attacking capability of a long-rod can be assessed from the derived relation as the rod impacts and penetrates the target with initial velocities of 300~1100 m/s. The results are compared with those of the experiments available in the open literature.

12.3 Constitutive Model of Concrete

The rapid development of computer technology and numerical techniques has provided a powerful tool in the numerical analysis of concrete structures. The material behavior is often expressed by a constitutive law, which should be invoked (Alves, 2000). Once the numerical method is determined, the loading condition and material model are two of the most important points in the numerical simulation. The loading condition subjected to these reinforced concrete (RC) structures can be broadly categorized as two types, static loading and

dynamic loading. According to different loading cases, different numerical simulation methods and different material constitutive models for concrete are required.

In the numerical simulation, putting in place a realistic constitutive model for concrete turns out to be the remaining major obstacle in obtaining a reliable prediction. A lack of adequate models for concrete is one of the major factors hindering the extensive use of numerical methods for reinforced concrete structures. Against this background, the main objective of the present research is to develop a realistic constitutive model for concrete and then implement it in the numerical analysis.

In order to successfully analyze the response of concrete members, the constitutive model for concrete used in the simulation should be appropriate for the characteristics of concrete material under different loading cases. Concrete is a very complex material, consisting of mineral aggregate bound by cement paste containing a large amount of water and voids, which makes the behavior of reinforced concrete material rather complicated. The most important property of concrete material is that it is much weaker in tension compared with its compression strength and thus concrete material easily cracks. Then, cracked concrete shows strong nonlinear behavior. This nonlinear stress, strain behavior in a multiaxial stress state and the post-failure strain-softening behavior are the two most important complexities in modeling concrete material behavior. Because of these complexities, the development of a proper constitutive model describing concrete behavior under all conditions is still a very challenging task facing researchers.

In the constitutive model of concrete material, strength criterion is one of the key points. Although some empirical criteria for concrete such as the Willam-Warnke criterion, Ottosen criterion and Kotsovos-Palovic criterion have proposed practical solutions, a reliable material strength model with sound theoretical background is necessary. The recently developed Yu's unified strength theory (Yu's UST) theory, or twin-shear unified strength theory (TS-UST) (Yu, 1991; 1992; 2004) appeared to be promising. By varying the value of a controlling parameter b, Yu's UST theory encompasses many prevailing classic strength criteria as special cases. Though it has a strong mechanics concept, the meridian curve in UST theory is linear, which over-estimates the strength of concrete when it is under high pressure. Against this background, a modified UST theory is developed in the current study. The linear meridians in Yu's UST theory are replaced by empirical curves, meaning Kotsovos' compressive and tensile meridian curves (Kotsovos and Pavlovic, 1995). This logical step leads to a robust semi-empirical, semi·theoretical strength model.

Based on the failure criteria, the concept of a Multi-Surface Strength (MSS) model is developed by Zhou (2002). According to this MSS model, the stress state in concrete can be divided into different stress regions. Inside those regions, different stress-strain relations are constructed accordingly. Based on the concept of the MSS model, both static and dynamic material models for concrete have been developed in the present study.

The mathematical equations of the unified strength theory are

$$F=\sigma_1-\frac{\alpha}{1+b}(b\sigma_2+\sigma_3)=\sigma_t, \text{ when } \sigma_2\le\frac{\sigma_1+\alpha\sigma_3}{1+\alpha}, \tag{12.1a}$$

$$F'=\frac{1}{1+b}(\sigma_1+b\sigma_2)-\alpha\sigma_3=\sigma_t, \text{ when } \sigma_2\ge\frac{\sigma_1+\alpha\sigma_3}{1+\alpha} \tag{12.1b}$$

The three principal stresses can be written in terms of the stress tensor invariant as

$$\begin{Bmatrix}\sigma_1\\ \sigma_2\\ \sigma_3\end{Bmatrix}=\begin{Bmatrix}s_1\\ s_2\\ s_3\end{Bmatrix}+\frac{I_1}{3}\begin{Bmatrix}1\\ 1\\ 1\end{Bmatrix}=\frac{2\sqrt{J_2}}{\sqrt{3}}\begin{Bmatrix}\cos\theta\\ \cos(\theta-2\pi/3)\\ \cos(\theta+2\pi/3)\end{Bmatrix}+\frac{I_1}{3}\begin{Bmatrix}1\\ 1\\ 1\end{Bmatrix} \tag{12.2}$$

with $\sigma_1\ge\sigma_2\ge\sigma_3$.

Therefore, the unified strength theory Eqs. (12.1a) and (12.1b) can be re-written in terms of the invariant notations as

$$F_1=\frac{I_1}{3}(1-\alpha)+(1+\frac{\alpha}{2})\frac{2}{\sqrt{3}}\sqrt{J_2}\cos\theta+\frac{\alpha(1-b)}{1+b}\sqrt{J_2}\sin\theta=f_t$$
$$\text{when} \quad 0\le\theta\le\theta_b, \tag{12.3a}$$

$$F_2=\frac{I_1}{3}(1-\alpha)+(\frac{2-b}{1+b}+\alpha)\frac{1}{\sqrt{3}}\sqrt{J_2}\cos\theta+(\alpha+\frac{b}{1+b}r)\sin\theta=f_t$$
$$\text{when} \quad \theta_b\le\theta\le 60° \tag{12.3b}$$

where I_1 is the first stress invariant, J_2 is the second deviatoric stress invariant and θ_b is the angle of an angular point of trajectory in the deviatoric plane, which can be calculated from F_1=F_2

$$\theta_b=\arctan\frac{\sqrt{3}}{2\alpha+1} \tag{12.4}$$

The first stress invariant I_1 can be calculated by $I_1=\sigma_{ii}$, where σ_{ii} is the stress tensor. The second deviatoric stress invariant $J_2=s_{ij}s_{ij}/2$.

The serial yield loci of the unified strength theory and its special case with b=0.6 are shown in Fig. 12.3.

The yield surface is defined exactly in the same way as the failure surface except that the ultimate tensile strength f_t (in Eqs. (12.3a) and (12.3b)) is replaced by a smaller strength, which defines the elastic limit, namely "yield" strength.

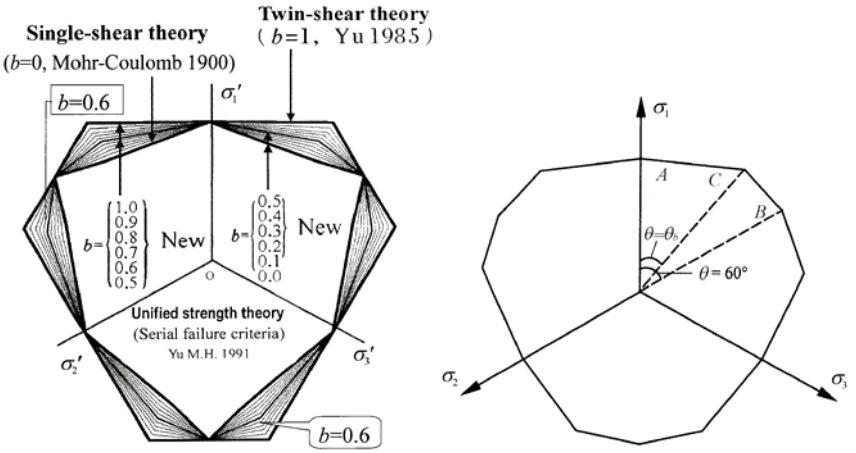

Fig. 12.3 Yield loci of the unified strength theory and its special case with b=0.6

Loading Surface and Work Hardening

Prior to yielding, concrete materials are generally assumed to be in the linear elastic state. Beyond initial yielding, the stress level at which further plastic deformation occurs may be dependent on the current degree of plastic strain. Such a phenomenon is termed 'work hardening' or 'strain hardening'. Therefore, the yield surface will vary at each stage of the plastic deformation and all these subsequent yield surfaces are called "loading surfaces". The progressive development of the loading surfaces can be defined by relating the stresses to the plastic deformation by means of a hardening parameter

$$f(\sigma_{ij}) = K(k) \tag{12.5}$$

where f is a stress function which represents a specific stress level, K is a function of the hardening parameter k and $\sigma_{ij}(i, j=1,2,3)$ are the components of the stress tensor. Equation (12.5) generates a loading surface in a 3D stress state.

The hardening parameter can be defined in two ways, namely 'work hardening' and 'strain hardening'. In this chapter 'work hardening' is used. The degree of 'work hardening' can be postulated as a function of the total plastic work only. Then

$$k = W_p \tag{12.6}$$

where

$$W_p = \int \sigma_{ij}(\mathrm{d}\varepsilon_{ij})_p \tag{12.7}$$

in which $(\mathrm{d}\varepsilon_{ij})_p$ are the plastic components of strain occurring during a strain increment. The stress states, when f=k, represent plastic states, while elastic

behavior is characterized by $f<k$. In a plastic state, the incremental change in the yield function due to an incremental stress change is

$$\mathrm{d}f = \frac{\partial f}{\partial \sigma_{ij}} \mathrm{d}\sigma_{ij} \tag{12.8}$$

Then, if

$f<0$, elastic unloading occurs and the stress point returns inside the yield surface;

$f=0$, means neutral loading and the stress point remains on the yield surface;

$f>0$, means plastic loading and the stress point remains on the expanding yield surface.

Elasto-Plastic Stress-Strain Relation

Beyond initial yielding, the material behavior will be partly elastic and partly plastic. At an increment of stress, the changes in strain are assumed to be decomposed into two components: elastic and plastic components such that

$$\mathrm{d}\varepsilon_{ij} = (\mathrm{d}\varepsilon_{ij})_e + (\mathrm{d}\varepsilon_{ij})_p \tag{12.9}$$

The elastic strain increment is related to the stress increment. It is assumed that the plastic strain increment is proportional to the stress gradient of the plastic potential g, such that

$$(\mathrm{d}\varepsilon_{ij})_p = \mathrm{d}\lambda \frac{\partial g}{\partial \sigma_{ij}} \tag{12.10}$$

where $\mathrm{d}\lambda$ is a proportional constant. According to the associated theory of plasticity, it becomes

$$(\mathrm{d}\varepsilon_{ij})_p = \mathrm{d}\lambda \frac{\partial f}{\partial \sigma_{ij}} \tag{12.11}$$

where f is the yield function.

Rearranging the yield function Eq. (12.5) leads to

$$F(\sigma_{ij}, \kappa) = f(\sigma_{ij}) - K(\kappa) = 0 \tag{12.12}$$

Differentiating Eq. (12.12), we have

$$\mathrm{d}F = \frac{\partial F}{\partial \sigma_{ij}}\mathrm{d}\sigma_{ij} + \frac{\partial F}{\partial \kappa}\mathrm{d}\kappa = 0 \tag{12.13}$$

or

$$\{a\}^{\mathrm{T}}\mathrm{d}\sigma_{ij} - A\mathrm{d}\lambda = 0 \tag{12.14}$$

where $\{a\}^{\mathrm{T}}$ is the flow vector, defined as the partial derivative of F with respect to the stress tensor

$$\{a\}^{\mathrm{T}} = \frac{\partial F}{\partial \sigma_{ij}} = [\frac{\partial F}{\partial \sigma_{11}}\frac{\partial F}{\partial \sigma_{22}}\frac{\partial F}{\partial \sigma_{33}}\frac{\partial F}{\partial \sigma_{12}}\frac{\partial F}{\partial \sigma_{23}}\frac{\partial F}{\partial \sigma_{31}}] \tag{12.15}$$

and

$$A = -\frac{1}{\mathrm{d}\lambda}\frac{\partial F}{\partial \kappa}\mathrm{d}\kappa \tag{12.16}$$

Substituting Eq. (12.11) into Eq. (12.9) leads to

$$\mathrm{d}\varepsilon_{ij} = [D]^{-1}\mathrm{d}\sigma_{ij} + \mathrm{d}\lambda\frac{\partial F}{\partial \sigma_{ij}} \tag{12.17}$$

where [D] is the usual matrix of elastic constants. By pre-multiplying both sides of Eq.(12.17) by $\{a\}^{\mathrm{T}}[D]$ and eliminating $\{a\}^{\mathrm{T}}\mathrm{d}\sigma_{ij}$ through Eq.(12.14), the plastic multiplier $\mathrm{d}\lambda$ can be obtained as (also Eq. (5.48) in Chapter 5)

$$\mathrm{d}\lambda = \frac{1}{A + \{a\}^{T}[D]\{a\}}\{a\}^{T}[D]\mathrm{d}\{\varepsilon\} \tag{12.18}$$

Substituting Eq. (12.18) into Eq. (12.17) leads to the complete elasto-plastic incremental stress-strain relation such that

$$\mathrm{d}\sigma_{ij} = [D]_{ep}\mathrm{d}\varepsilon_{ij} \tag{12.19}$$

where the matrix of elasto-plastic constants is expressed as (also Eq. (5.50) in Chapter 5)

$$[D]_{ep} = [D] - \frac{[D]\{a\}\{a\}^{\mathrm{T}}[D]^{\mathrm{T}}}{A + \{a\}^{\mathrm{T}}[D]\{a\}} \tag{12.20}$$

From a thermodynamic viewpoint, the work hardening hypothesis is more general than the strain hardening hypothesis. Therefore, the work hardening

hypothesis is used here,

$$\mathrm{d}\kappa = [\sigma]^{\mathrm{T}}\,\mathrm{d}\{\varepsilon\}_p \tag{12.21}$$

With this hypothesis we can obtain

$$A = H' \tag{12.22}$$

where H' is the hardening parameter which can be determined experimentally from a simple uniaxial test.

Flow Vector for Numerical Computation and Processing of Corner Singularity

As an alternate form of Eq. (12.15), the flow vector can also be expressed as

$$\{a\} = \frac{\partial F}{\partial \{\sigma\}} = \frac{\partial F}{\partial I_1}\frac{\partial I_1}{\partial \{\sigma\}} + \frac{\partial F}{\partial \sqrt{J_2}}\frac{\partial \sqrt{J_2}}{\partial \{\sigma\}} + \frac{\partial F}{\partial \theta}\frac{\partial \theta}{\partial \{\sigma\}} \tag{12.23}$$

where

$$\{\sigma\}^{\mathrm{T}} = \{\sigma_{11}\sigma_{22}\sigma_{33}\sigma_{12}\sigma_{23}\sigma_{31}\}$$

When UST theory is used to define the loading surfaces, the flow vector is not uniquely defined at the demarcation points. It occurs at θ=0, θ=60° and θ=θ_b. The corresponding points are A, B and C as shown in Fig. 12.4.

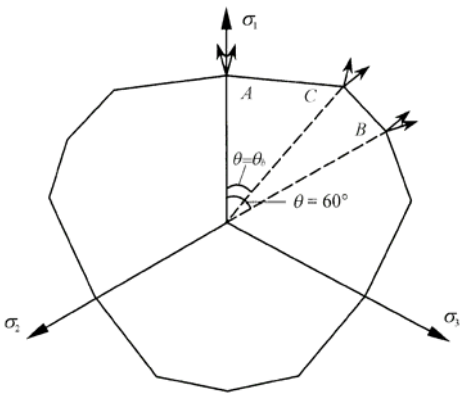

Fig. 12.4 Singular points of UST with b=0.6 in the deviatoric plane

It is worth noting that there are two exceptional cases：(1) When b is equal to 1, points A and B are not angular points (see Fig. 12.2). Hence the flow vectors at A and B can be used without any processing. (2) When b is equal to 0, point C is not a singular point (Fig. 12.2) and, accordingly, the corresponding flow vector can be

used without any processing. However, in other cases ($b\neq0$, $b\neq1$), these comer singularities exist. To overcome these, one simple method is to approximate the flow vectors using those in the exceptional cases. That is, the flow vectors at A and B for all cases ($0\leq b\leq1$) are the same as those for b=1. Similarly, the flow vectors at C for all cases ($0\leq b\leq1$) are the same as those for b=0. The expressions for C_1, C_2, and C_3 for these comers are the same as the description in Chapter 5.

The flow vectors for numerical computation and processing of corner singularity are the same as the processing described in Chapter 5 (Eqs. (5.45) to (5.99)). The corresponding flow vectors are shown in Fig. 12.3.

The UST is generalized to the damage surface study (Zhou, 2002), as shown in Fig. 12.5.

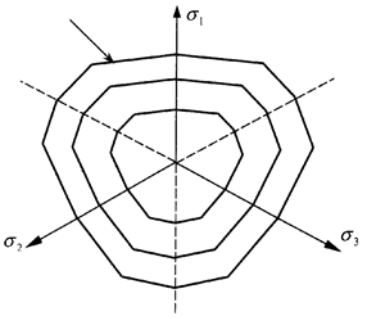

Fig. 12.5 Damage surface based on the UST with b=0.6

The dynamic material model for concrete in the present study aims to simulate concrete behavior against penetration. The subject of penetration and perforation has long been of interest in the military field, but it still needs further study because of its complexity. It is a well-known fact that concrete exhibits a rate dependent behavior when subjected to high-speed dynamic loading. As compared with the measured parameters in static tests, it shows a significant increase in dynamic strength and a decrease in non-linearity of the stress-strain response curves. This peculiar behavior is very important under impulsive loading because it dominates the responses of the structure when subjected to impacts (with strain rates $\dot{\varepsilon}>10^{-2}$ s^{-1}). Observations by others show that the rate-sensitivity is mainly due to the fact that the growth in internal microcracking (for a particular level of strain) is retarded at higher strain-rates. Knowing that the damage to concrete is essentially due to the nucleation and growth of micro voids and micro-cracks, one can deduce that diminishing micro-cracks due to an increasing strain rate will result in a reduction in macroscopic nonlinear behavior and also an increase in dynamic strength (Cervera et a1., 1996). Therefore, material models for concrete should be different between the static loading case and dynamic loading case. In other words, the strain rate effect needs to be considered in the dynamic material model for concrete.

In the MSS models developed in the present study, the plastic model and

damage variable are combined to treat the response of concrete at different stress stages. The pre-failure behavior of concrete is modeled by elasto-plastic theory, while the damage model is introduced to treat the post-failure response in order to take account of the degradation of both strength and stiffness. The differences between the static and dynamic versions lie in the definition of the failure surface and the post-failure treatments. In the dynamic version, the strain-rate effect is included in defining the failure surface. In addition, the post-failure behavior follows a kind of isotropic damage model, in which the damage scale is a measure of the accumulated equivalent plain strain. Of course, in the static version no strain-rate effect is considered and the post-failure treatment adopts the Mazars damage model (Mazars, 1986), in which the damage parameter is a measure in the direction of principle stress.

To test and verify Yu's UST-based static models for concrete, some RC beams under static loading are calculated and compared with experimental results. Both two dimensional (2D) and three dimensional (3D) simulations of perforation through a concrete slab are presented to verify the dynamic material model for concrete. These numerical examples show that both the static and the dynamic material models for concrete can be used to simulate the response of a concrete member under different loading cases.

12.4 Penetration and Perforation of Reinforced Concrete Slab

To verify and calibrate the dynamic material model for concrete proposed by Zhou based on the UST and damage theory, numerical simulations were carried out (Zhou, 2002). The specific impact configuration in the experiments set up by Hanchak et al. (1992) was adopted. The target was a 610 mm×610 mm square panel of l78 mm thick reinforced concrete slab. The projectile was an ogival nose shaped 143.7 mm long steel rod having a diameter of 25.4 mm and a 3.0 caliber-radius-head. Hanchack conducted his tests over a range of impact velocities between 300 and 1000 m/s.

Figures 12.6 and 12.7 show the nominal geometric configurations of the steel projectile and the concrete target in Hanchack's tests. An axisymmetric analysis was carried out in the numerical simulation, in which the target is a circular panel of 688.4 mm in diameter. Since the target panel was only lightly reinforced, the effect of the reinforcement would be negligible provided that the projectile impacted on the target somewhere near the center of a space in the reinforcement grid. For this reason, the steel reinforcement bars are not included in the numerical model.

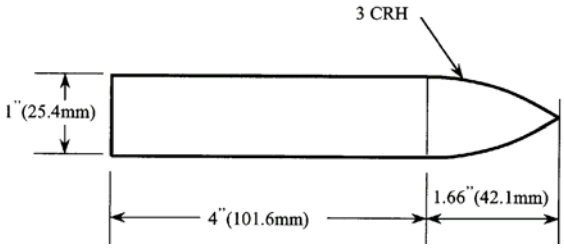

Fig. 12.6 Geometry of the steel projectile

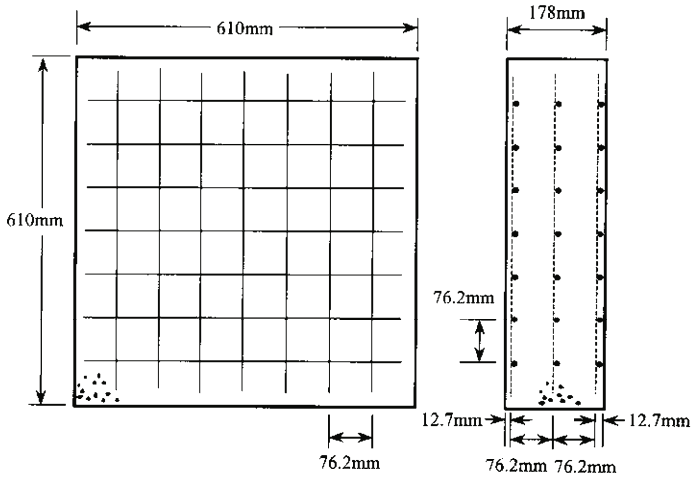

Fig. 12.7 Configuration of concrete target (Zhou, 2002)

The finite element mesh is shown in Fig. 12.8. The mesh for the target has 8000 quadrilateral elements and 8181 nodes. The mesh for the projectile has 504 elements and 559 nodes. Due to symmetry, only half of the target-and-projectile configuration is analyzed.

Post-experimental observations showed little or no damage was inflicted on the projectile. Therefore, as the first-order approximation, the steel projectile was modeled as an elastic-perfectly-plastic material having the following properties (Hanchak et al., 1992): mass density 8020 kg/m^3, bulk modulus 175 GPa, shear modulus 80.8 GPa and yield stress 1.72 GPa. The Huber-von Mises criterion is used as yield criterion for the steel projectile.

Two grades of concrete target were used in the experiments by Hanchak et al. (1992). One set of targets has an unconfined compressive strength of 48.0 MPa while the other set is 140.0 MPa. Only the lower strength concrete target is analyzed here. The material parameters used in the present simulation are shown in Tables 12.1 and 12.2. The piece-wise-linear plastic compaction path for the EOS is defined by five pairs of density to pressure values. Table 12.1 gives the values of these five pairs.

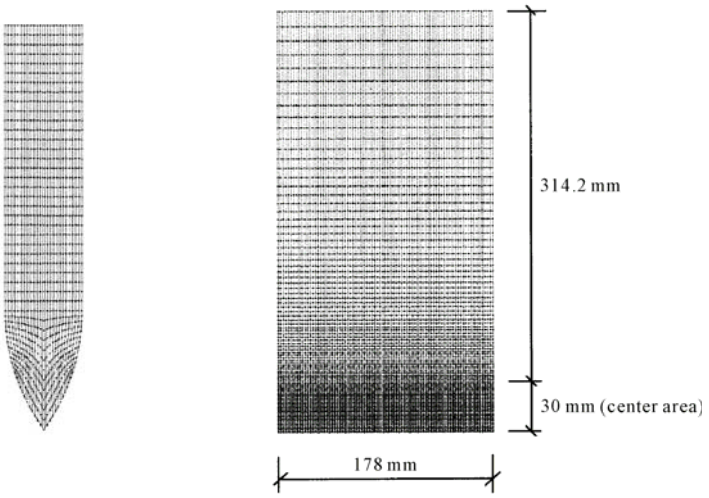

(a) Projectile (b) Target

Fig. 12.8 The finite element mesh of the steel projectile and concrete target (Zhou, 2002)

Figure 12.9 shows Hanchack's experimental results of pressure versus volumetric strain and the approximated linearization adopted in Zhou's study (Zhou, 2002).

During the perforation process, some of the Lagrangian elements in the concrete target can become grossly distorted and, unless some remedial actions are taken, can seriously impair the progress of the calculation. To alleviate this problem, a numerical mechanism namely "erosion algorithm" is put in place in the hydrocode Auto-DYNA. A pre-defined strain value is set as the limit strain, beyond which the highly distorted elements will be removed as it progresses. In the present study, erosion is initiated by an incremental geometric strain limit, and a strain value of 300% is set as the limit.

Table 12.1 General material parameters for the concrete target

Parameter	Value	Parameter	Value
Reference density	2430 kg/cm^3	Shear modulus	12.5 GPa
Solid sound speed	2600 m/s	Porous sound speed	2600 m/s
Compressive strength	48 MPa	H'_c	18 GPa
Tensile strength	4 MPa	E	28 GPa
Parameter b of UST	0.6	D_1	0.03
K_{c0}	0.5	D_2	1
K_{f0}	0.9	P_{l0}	40 MPa
H'_t	18 GPa	P_{u0}	55 MPa

Table 12.2 Piece-wise linear porous EOS (pressure versus density)

Density (kg/m^3)	Pressure (MPa)
2305	0
2311.5	30
2321.5	70
2409.1	350
2471.3	644

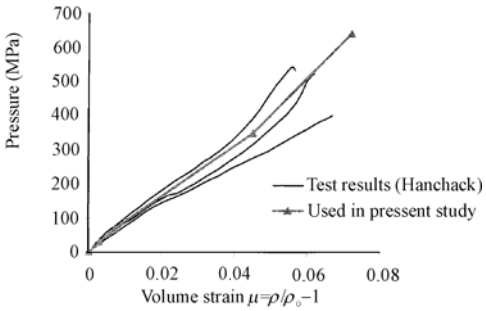

Fig. 12.9 Pressure versus volumetric strain

Hanchack reported his test results with four impact velocities, 1058 m/s, 750 m/s, 434 m/s, 300 m/s. Simulations for these four cases were carried out using Zhou's model i.e. the combination of the UST with b=0.6 and damage theory. Figure 12.10 shows the impact velocities versus the residual velocities and compared with Hanchack's results too. Table 12.3 lists the corresponding numerical values. The velocity of the projectile decreases clearly along its path of penetration. The resisting forces arise from the inertia and strength of the target material. Upon perforation, the projectile decouples from the target and its velocity becomes constant. That constant velocity is defined as the residual (or exit) velocity of the projectile. If perforation does not occur, the projectile rests and embeds itself inside the target with zero residual velocity.

Table 12.3 Comparison of exit velocities for perforation of normal RC slab

Impact velocity (m/s)	Exit velocity (m/s) (test result)	Exit velocity (m/s) (numerical result)	Error (%)
300	0	57	——
434	214	219	2.34
750	610	593	2.79
1058	947	920	2.85

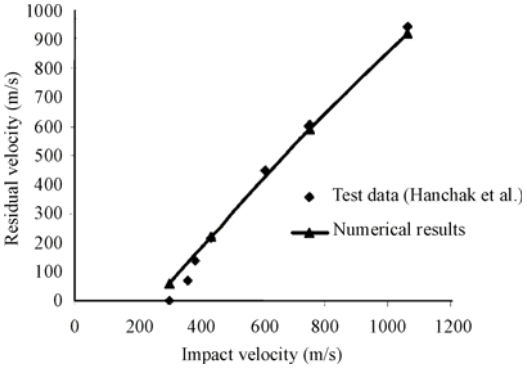

Fig. 12.10 Impact velocity versus residual velocity for test data and numerical results

From Fig. 12.10 and Table 12.3, it can be seen that numerical simulations are in good accord with the experimental results. Apart from the impact velocity of 300 m/s, the relative errors of the numerical results are less than 3%. It is worth noting other details. For illustrative purposes, further details for the case when the impact velocity is 750 m/s are discussed. The detailed procedure of the penetration is also obtained. The contour plots of damage in the concrete target at different time cycles are shown in Fig. 12.11 (Zhou, 2002).

12.5 Perforation of Fibre Reinforced Concrete Slab

Zhou's material model combined with the UST and test data is employed to simulate a fiber-reinforced concrete target. Experiment results are reported by Hansson et al. (2000). The target is a 1.2 m×l.2 m square slab of 0.06 m thick fiber-reinforced concrete, having an unconfined compressive strength of 79.5 MPa and a splitting tensile strength of 7.4 MPa. The modulus of elasticity was taken to be 52.9 GPa and the density 2330 kg/m^3. The projectile is a 43 mm long solid cylinder, having a diameter of 15 mm and a weight of 60 g. It was fabricated from steel SS l4 2541-03 having a 0.2% proof strength of 700 MPa and an ultimate strength between 900 and l l00 MPa. Experimental data are available for two shots fired against the slab at an impact velocity of l637 m/s and l505 m/s respectively.

Since the penetration/perforation process is a highly localized event, it can be simply reduced to a 2D axisymmetrical analysis. As such, the square slab is replaced by a circular plate having a radius of 500 mm. By making use of symmetry, only half of the target-and-projectile section is analyzed. The domain of the target is discretized into 60×100 elements in the finite element model. The size of the element mesh increases gradually and radially away from the center. The projectile is discretized into 44×16 elements. In order to reduce the effect of stress wave reflections from the boundary, a transmissible boundary condition is applied along the peripheral boundaries of the slab.

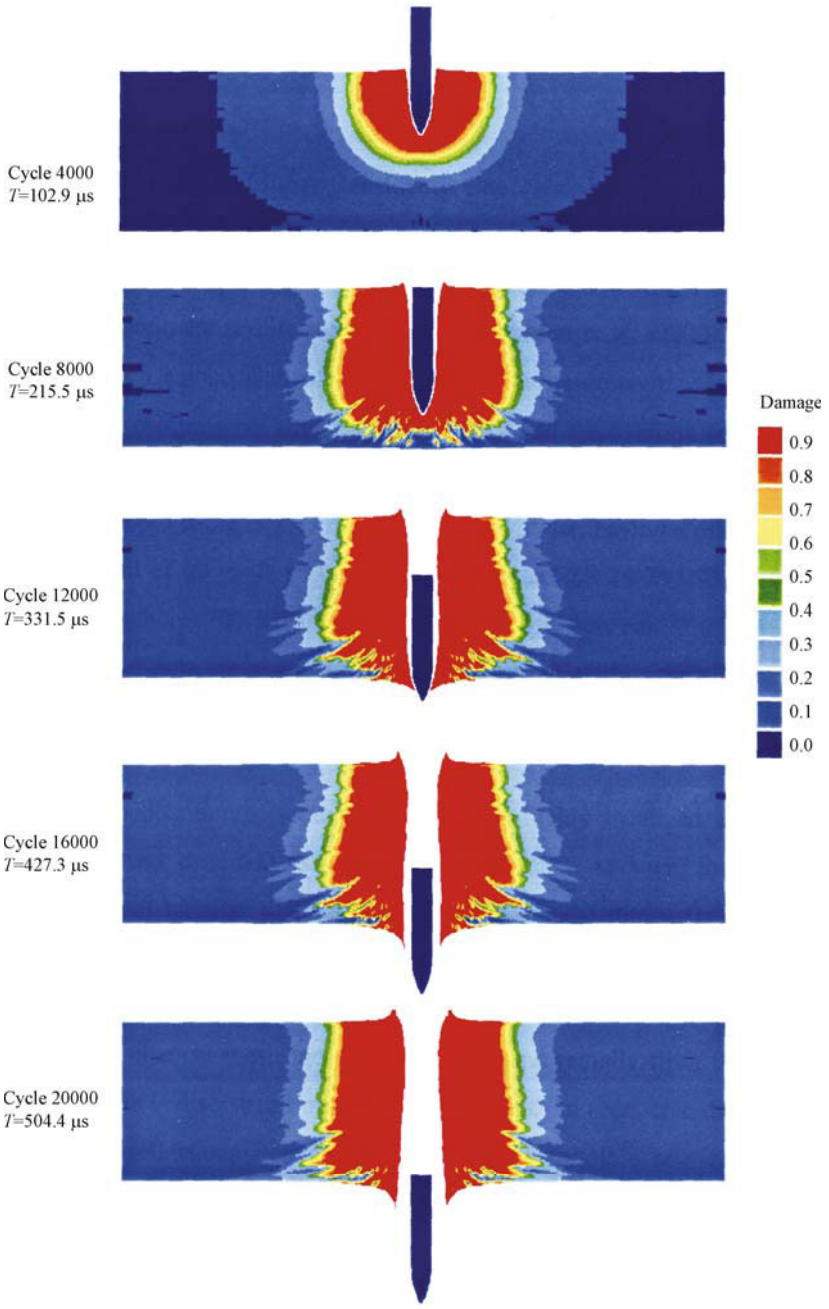

Fig. 12.11 Contour plot of damage at different cycles (v=750 m/s) (Zhou, 2002)

The fiber reinforced concrete is treated as a homogeneous material having similar but slightly different properties, as shown in Table 12.4. The projectile is modeled according to the Johnson & Cook material model for steel. The mechanical properties are based on the typical data for 4340 steel. The material parameters for the steel projectile are shown in Table 12.5 In the simulation, an erosion strain of 500% is adopted.

Table 12.4 General material parameters for the fiber RC target

Parameter	Value	Parameter	Value
Reference density	2410 kg/cm^3	Shear modulus	20.8 GPa
Solid sound speed	2900 m/s	Porous sound speed	2900 m/s
Compressive strength	795 MPa	H'_c	32 GPa
Tensile strength	7.4 MPa	E	50 GPa
UST parameter b	0.6	D_1	0.03
K_{co}	0.5	D_2	1
K_{fo}	0.9	P_{lo}	80 MPa
H'_t	32 GPa	P_{uo}	115 MPa

Table 12.5 Piece-wise linear porous EOS (pressure versus density)

Density(kg/m^3)	Pressure(MPa)
2330	0
2336	20
2346	48
2390	380
2452	650

Simulations are carried out for the two shots having an impact velocity of l503 m/s and l637 m/s. The velocity-history plots for the projectile are shown in Fig. 12.10 and Fig. 12.11, respectively. It can be observed that during the perforation process the velocity of the projectile decreases readily. Upon perforation, the velocity becomes constant. Table 12.6 shows the comparison of exit velocities between the numerical simulations and the test results. Good agreements are observed. Figure 12.12 shows the contour plots of damage at different time steps.

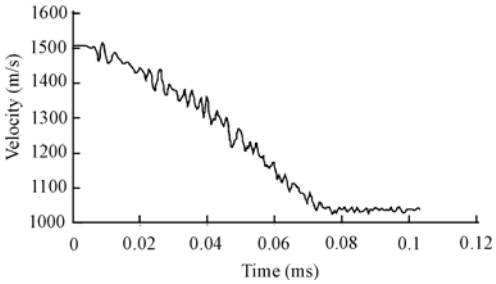

Fig. 12.12 Velocity history of projectile (Fiber RC slab, v=1 5 05 m/s)

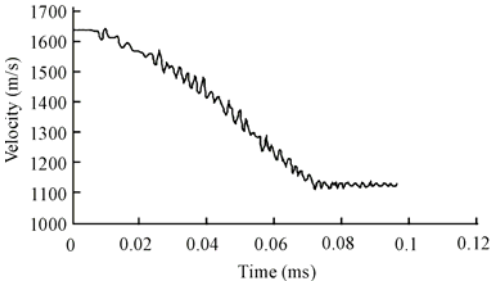

Fig. 12.13 Velocity history of projectile (Fiber RC slab, v=1 637 m/s)

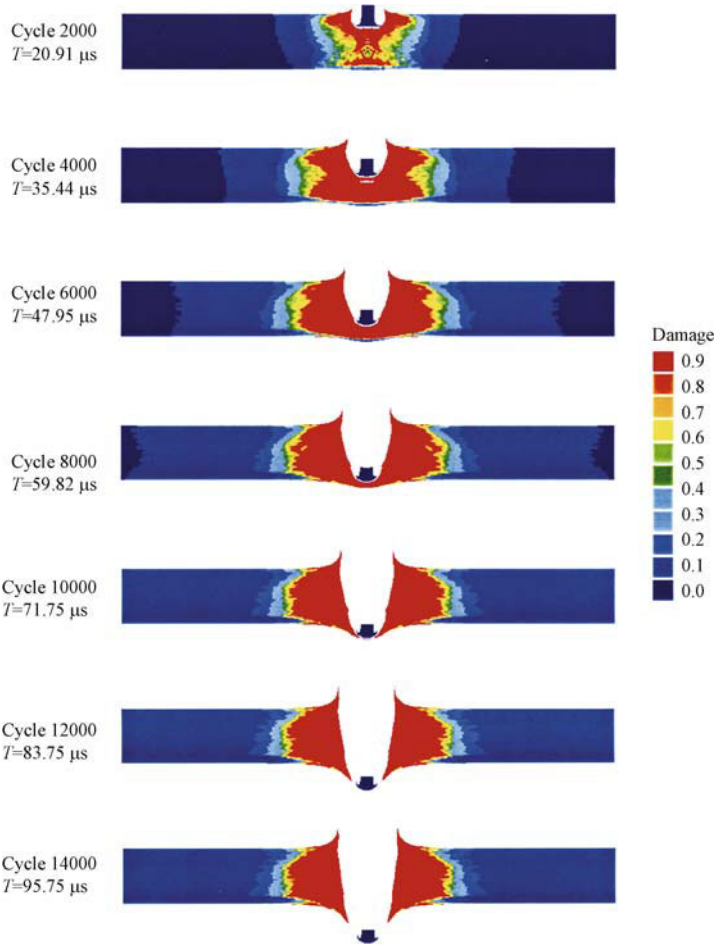

Fig. 12.14 Contour plot of damage at different cycles for fiber RC slab (v=1503 m/s) (Zhou, 2002)

Table 12.6 Material constants for the steel projectile according to Johnson-Coak model

Material constant	Value
Reference density	7830 kg/m^3
Bulk modulus	1 59 GPa
Reference temperature	300 K
Specific heat	477 J/kg
Shear modulus	81.8 GPa
Yield stress	792 MPa
Gardening constant	510 MPa
Hardening exponent	0.26
Strain rate constant	0.014
Thermal softening exponent	1.03
Melting temperature	1793 K

Table 12.7 Comparison of exit velocities for perforation of fiber RC slab

Impact velocity v (m/s)	Exit velocity (m/s)	
	Experimental result	Present simulation
1505	1080	1036
1637	1120	1130

12.6 High Velocity Impact on Concrete Slabs Using UST and SPH Method

The Smoothed Particle Hydrodynamics (SPH) method was first applied by Lucy (1977) to astrophysical problems and was extended by Gingold and Monaghan (1982). Cloutman (1991) has shown that SPH could be used to model hypervelocity impacts. Libersky and Petschek (1991) have shown SPH can be used to model material with strength. Liu et al. (2003) have studied blasting simulation with explosives in fluid media and Liu (2002) has reviewed mesh free methods and introduced this method systematically. In fact, SPH is a gridless Lagrangian technique. The main advantage of the method is to bypass the requirement for a numerical grid to calculate spatial derivatives. This avoids the severe problems associated with mesh tangling and distortion which usually occur in Lagrangian analyses involving large deformation impact and explosive loading events. The grid based methods, such as Lagrange and Euler, assume a connectivity between nodes to construct spatial derivatives. SPH uses a kernel approximation, which is based on randomly distributed interpolation points with no assumptions about which points are neighbours, to calculate spatial derivatives. Here, a dynamic plastic damage model is proposed by Prof. Fan SC and Qiang using UST (Unified Strength theory) and on an RHT concrete model (Riedel et al., 1999). The research was presented by Prof. Fan SC at Sydney, Australia in 2001 (Fan and Qing, 2001) and described below.

12.6.1 Material Model for the Concrete Slab

Dynamic multi-limit surface models based on the unified strength theory are employed here, i.e. the elastic limit surface, failure surface and residual strength surface. The failure surface is a bounding surface, no stress state is allowed to exist beyond it. The shapes of the failure surface could be changed in the stress space during the impact process. However, the loading surface changes its shape non-uniformly from the initial surface to the failure surface with the development of the effective plastic strain. Once the failure surface is reached, the residual strength surface is determined according to the scalar damage value.

Based on this consideration, the dynamic material model is proposed. The main characteristics of this model are:

1) Strain-rate dependent failure surface is considered.
2) UST theory is employed in the failure surface.
3) Linear strain hardening is used to impose the plastic flow consideration.
4) Isotropic damage is used in this model due to increased strain after the stress in the reached failure surface.

12.6.2 The Failure Surface

Amongst the strength models available, UST theory has a clear mechanical concept and simple mathematical formula. The advantage of the UST theory is that it takes account of the second principal stress on the material strength. However, the Huber-von Mises criterion is based on the average principal stresses while the Mohr-Coulomb criterion neglects the intermediate principal stresses. The envelope is then completed by defining a piece-wise linear interpolation function in the deviatoric plane. The beauty of the twin-shear-unified strength theory is its feasibility in defining the convex shape of the surface. Setting the value of the controllable convex parameter b to 0 or 1 yields the lower and upper limit of the convex shape function. For any arbitrary value of b, the shape function can be written in the following form.

$$R_f = \frac{r_t r_c \sin 60^\circ}{r_t \sin\theta + r_c \sin(60^\circ - \theta)}(1-b) + b\frac{r_t}{\cos\theta} \quad \text{when} \quad 0^\circ \le \theta \le \theta_b \tag{12.24a}$$

$$R_f = \frac{r_t r_c \sin 60^\circ}{r_t \sin\theta + r_c \sin(60^\circ - \theta)}(1-b) + b\frac{r_t}{\cos(60^\circ - \theta)} \quad \text{when} \quad \theta_b \le \theta \le 60^\circ \tag{12.24b}$$

where J_2 and J_3 are the second and third stress invariants respectively, r_t and r_c are the tensile and compressive meridians respectively.

$$\theta_b = \arctan\left[\frac{1}{\sqrt{3}}\left(\frac{2r_c}{r_t}-1\right)\right], \cos 3\theta = \frac{3\sqrt{3}}{2}\frac{J_3}{\sqrt{J_2^3}} \tag{12.25}$$

It is worth noting that the unified strength theory parameter b reflects the influence of the intermediate principal stress on the material strength. Besides, it encompasses all prevailing yield or failure criteria. When b=0 it can represent the Tresca criterion; when b=0.5 it is equivalent to the Huber-von Mises criterion. The shapes represented by different values of b in the deviatoric plane and multi-limit surface in the meridian plane are shown in Fig. 12.15 and Fig. 12.16. In the present investigation, the unified strength theory parameter b is set to b=0.6.

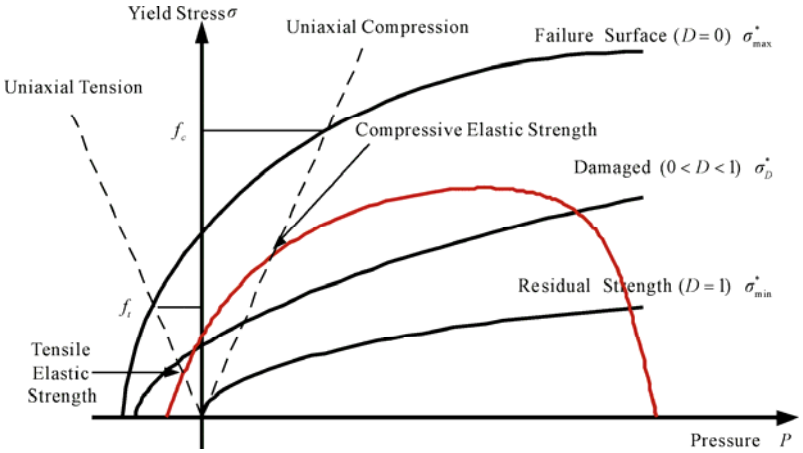

Fig. 12.15 Multi-limit surface in meridian projection

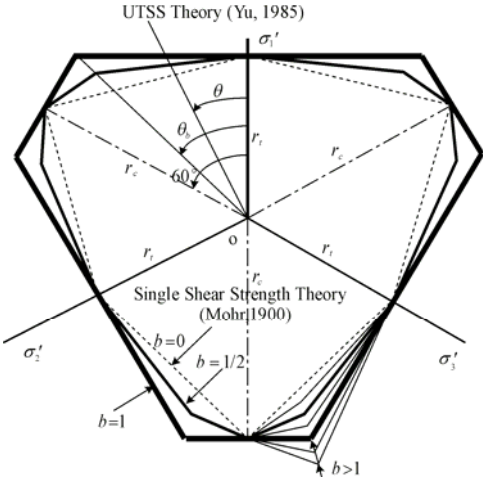

Fig. 12.16 Multi-limit surface in deviatoric projection

The failure surface is defined as a function of pressure P, the Lode stress angle θ and strain rate $\dot{\varepsilon}$.

$$Y_{fail} = Y_{TXC(P)} \cdot R_f \cdot F_{RATE(\dot{\varepsilon})} \tag{12.26}$$

where $Y_{TXC} = f_c \left| A(P^* - P^*_{spall} F_{RATE})^N \right|$, in which f_c is compressive strength; A is failure surface constant; N is failure surface exponent; P^* is pressure normalized by f_c; P^*_{spall} is defined as $P^*(f_t / f_c)$.

$$F_{RATE} = \begin{cases} \left(\dfrac{\dot{\varepsilon}}{\dot{\varepsilon}_0} \right)^D & \text{for} \quad P > \dfrac{1}{3} f_c \quad \text{(compression)} \\ \left(\dfrac{\dot{\varepsilon}}{\dot{\varepsilon}_0} \right)^a & \text{for} \quad P < \dfrac{1}{3} f_t \quad \text{(tension)} \end{cases}$$

in which D is the compressive strain rate factor exponent; a is the tensile strain factor exponent.

12.6.3 The Elastic Limit Surface

The elastic limit surface is scaled from the failure surface using

$$Y_{elastic} = Y_{fail} \cdot F_{elastic} \cdot F_{CAP(P)} \tag{12.27}$$

where $F_{elastic}$ is the ratio of the elastic strength to failure surface strength. This is derived from two material parameters, tensile elastic strength f_t and compressive elastic strength f_c. $F_{CAP(P)}$ is a function that limits the elastic deviatoric stresses under hydrostatic compression via

$$F_{CAP} = \begin{cases} 1 & \text{for} \quad P \le P_u \\ \sqrt{1 - \left(\dfrac{P - P_u}{P_0 - P_u} \right)^2} & \text{for} \quad P_u < P < P_0 \\ 0 & \text{for} \quad P_0 < P \end{cases} \tag{12.28}$$

12.6.4 Strain Hardening

Linear hardening is used prior to the peak load. During hardening, the current yield surface (Y^*) is scaled between the elastic limit surface and the failure surface via

$$Y^* = Y_{elastic} + \frac{\varepsilon_{pl}}{\varepsilon_{pl(pre\text{-}softening)}}(Y_{failure} - Y_{elastic}) \tag{12.29}$$

where

$$\varepsilon_{pl(pre-softening)} = \frac{Y_{fail} - Y_{elastic}}{3G}\left(\frac{G_{elastic}}{G_{elastic} - G_{plastic}}\right).\ G_{elastic}/(G_{elastic} - G_{plastic})$$

is defined by the user.

12.6.5 Residual Failure Surface

A residual (frictional) failure surface is defined as

$$Y^*_{residual} = BP^{*M} \tag{12.30}$$

where B is the residual failure surface constant; M is the residual failure surface exponent.

12.6.6 Damage Model

Following on from the hardening phase, additional plastic straining of the material leads to damage and strength reduction, as shown in Fig. 12.5. The residual strength is described by a so-called "cumulative damage model" (Persson, 1990). Damage is accumulated via

$$D = \sum \frac{\Delta\varepsilon_{pl}}{\varepsilon_p^{failure}} \tag{12.31}$$

$$\varepsilon_p^{failure} = D_1(P^* - P^*_{spall})^{D_2} \geq \varepsilon_f^{\min} \tag{12.32}$$

where D_1 and D_2 are damage constants; $\varepsilon_f^{\min}$ is the minimum strain to failure.

The post-damaged failure surface is then interpolated via

$$Y^*_{fractured} = (1-D)Y^*_{failure} + DY^*_{residual} \tag{12.33}$$

and the post-damaged shear modulus is interpolated via

$$G_{fractured} = (1-D)G + DG_{residual} \tag{12.34}$$

where $G_{residual}$ is the G^*, the residual shear modulus fraction.

12.7 Numerical Example

To verify and calibrate the present model, a numerical simulation was carried out by Prof. Fan SC and Qiang (2001), which is to illustrate the results of the enhancements incorporated using the SPH method and UST model. It adopts the same configuration and materials used in the tests by Hanchak et al. (1992). The target is a 680 mm×680 mm square of a 178 mm thick reinforced concrete panel. The projectile is an ogival nose shaped 143.7mm long steel rod with a diameter of 25.4 mm and a 3.0 caliber-radius-head. The impact velocities vary between 300 and 1058 m/s. The experimental results are compared with simulation results in the present investigation, and the unconfined compressive strength of concrete is 48 MPa. For other parameters for the material model refer to Riedel et al. (1999).

In the simulation, both the projectile and the target regions are modeled using SPH. In order to simplify it to a 2D axisymmetric analysis, the square panel is approximated by a circular one of radius 303 mm. The target is discretized into 13528 particles while the projectile is represented by 1678 particles. The panel is lightly reinforced. However, Hanchak's results verify that the small amount of reinforcement does not have a major influence on the penetration resistance. Therefore, the steel bars are ignored in the modeling. An evenly spaced particle-model of SPH for concrete target and steel projectile is shown in Fig. 12.17.

The material model for the projectile adopts the linear EOS and the Johnson & Cook strength model. The mechanical properties are based on the AutoDYN's material library for steel 4340: initial density ρ_0=8.1 g/cm^3, bulk modulus K=159 GPa, shear modulus G=81.8 GPa, yield stress f_y=792 MPa etc.

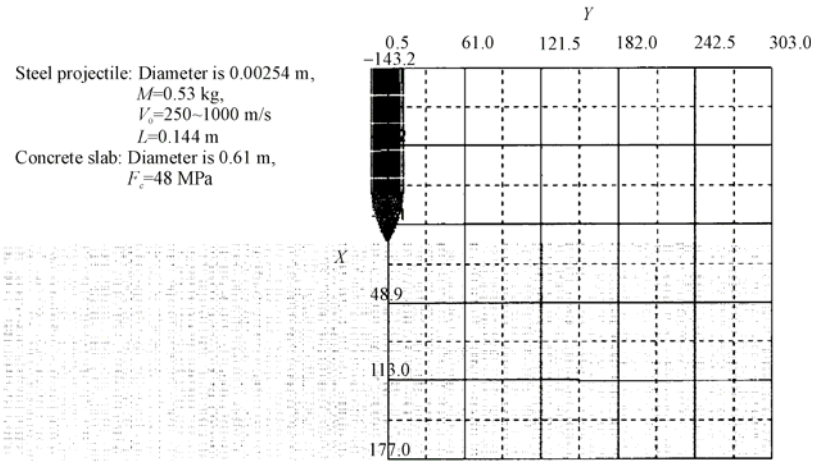

Fig. 12.17 Evenly spaced particle-model of SPH for concrete target and steel projectile

The same EOS is adopted for the concrete slab, only the bulk modulus K is different. The exit velocities and corresponding penetration depths of the projectile are shown in Table 12.8. The decrease in the velocity of the projectile is due to resistance by the target. After perforation (the target is a 680 mm×680 mm square, 178 mm thick), the velocity of the projectile remains constant because the target material can no longer offer any resistance (cases 1 and 2). This constant velocity is defined as the residual (or exit) velocity of the projectile. If perforation did not occur, the projectile would have come to rest and be embedded inside the target with zero residual velocity (case 4). Meanwhile, the reduction in the projectile velocity is recorded over the penetration depth and compared to the residual velocities measured in the normal strength concrete tests (f_c=48 MPa). At high initial velocities, the results of the dynamic constitutive law match the experimental values very closely. A ballistic limit of about 301 m/s is also correctly predicted in the simulation (case 4).

Table 12.8 Comparison of exit velocities and penetration depths

s/*n*	Impact velocity (m/s)	Exit (residual) velocity (m/s)		Simulation depths (mm)
		Test (Hanchak)	Simulation	
(1)	1058	947	950	178
(2)	749	615	625	178
(3)	360	67	71.5	174
(4)	301	0	0	163

The distribution of the compressive damage for the constitutive theory, with or without its dynamic part, emphasizes the importance of a realistic consideration of the strain-rate effect. In Fig. 12.18 the contour plots of the compressive damage

for time steps during a 750 m/s impact are shown. At the same time, the dynamic constitutive law exhibits a rather homogeneous damage distribution.

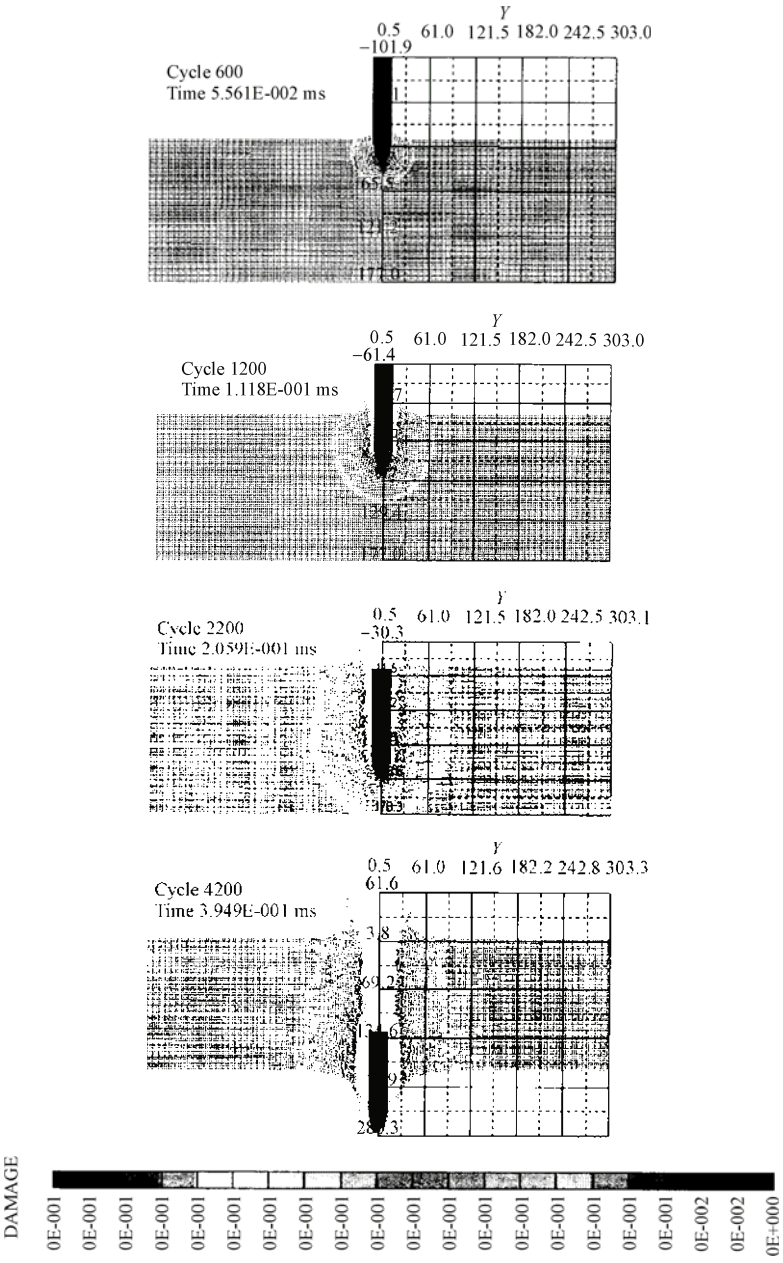

Fig. 12.18 Contour plots at selected time steps (Fan SC and Qiang, 2001)

The SPH procedure is employed by Fan and Qiang (2001) to simulate the impact-penetration process of a hard steel projectile onto/through a concrete target. A nonlinear equation of state and an improved strength criterion for concrete material are incorporated. The strength criterion takes account of the influence of the intermediate principal stress. The SPH procedure does not experience any numerical instability problem. The numerical simulations with the two enhancements yield results in good agreement with the experimental ones. The contour plot at the final step is shown in Fig. 12.19.

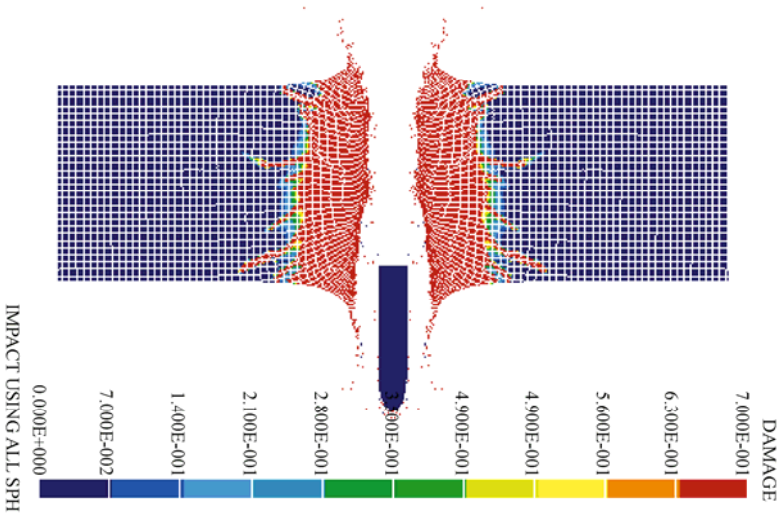

Fig. 12.19 Damaged contour plot at final step (Fan and Qiang, 2001)

12.8 Brief Summary

The UST (Unified Strength Theory) is implemented in AutoDYN and numerical examples of penetration of concrete slabs are given. The unified strength theory with parameter b=0.6 is used for simulation of penetration in three examples.

The numerical simulation of the penetration/perforation process of a concrete slab by a cylindrical steel projectile using the FE method and smoothed particle hydrodynamics (SPH) method is studied in this chapter. In the simulation, the available hydrocode AutoDYN-2D is employed with an improved RHT concrete model, in which unified strength theory (UST) or Yu's unified strength theory (Yu UST) is adopted in defining the material strength effects, and dynamic multifold limit/failure surfaces including elastic limit surface, failure surface and residual failure surface are constructed. The proposed model is incorporated into the AutoDYN hydrocode via the user

defined subroutine function. The results obtained from the numerical simulation are compared with available experimental ones. Good agreement is observed. It demonstrates that the proposed model can be used to predict not only the damaged areas and velocity reduction of the projectile during the perforation process, but also the debris clouds from the spalling process.

A multi-limit surface dynamic plastic damage model is developed based on the RHT model using UST theory. The present material model was coded and incorporated into AutoDYN. The numerical simulation was carried out for a case of perforation through a concrete slab by a steel projectile. Numerical results were compared with experimental results by others. They agreed favourably. It demonstrates that the present model could be used to predict not only the damaged areas and the velocity-decrease of the projectile during the perforation process but also the debris clouds from the spalling process, with an acceptable degree of accuracy.

References

Alves M (2000) Material constitutive law for large strain and strain rates. J. Engineering Mechanics, 126(2): 215-218.

AutoDYN (2000) Theory Manual. Century Dynamics Inc.

Cervera M, Oliver J and Manzoli O (1996) A rate dependent isotropic damage model for the seismic analysis of concrete dams. Earthquake Engineering and Structural Dynamics, 25: 987-1010.

Cloutman LD (1991) SPH simulations of hypervelocity impacts. Lawrence Livermore National Laboratory, UCRL-ID-105520.

Fan SC and Qiang HF(2001) Normal high-velocity impaction concrete slabs-a simulation using the meshless SPH procedures. In: Computational Mechanics– New Frontiers for New Millennium, Valliappan S. and Khalili N. eds. Elsevier Science Ltd., pp 1457-1462.

Gingold RA and Monaghan JJ (1982) Kernel estimates as a basis for general particle methods in hydrodynamics. Journal of Computational Physics, 46(4): 429-453.

Hansson H and Agardh L (2000) Experimental and numerical studies of projectile perforation in concrete targets. Structural Failure and Plasticity, Editors：Zhao XL and Grzebieta. Elsevier Science Ltd.115-120.

Hanchak SJ, Forrestal MJ, Young ER and Ehrgott JQ (1992) Perforation of concrete slabs with 40MPa and 140 MPa unconfined compressive strengths. Int. J. of Impact Engineering, 12(1):1-7.

Herrmarm W (1969) Constitutive equation for the dynamic companion of ductile porous material. J. of Applied Physics, 40(6): 2490-2499.

Jonas GH and Zukas JA (1978) Mechanics of penetration: analysis and experiment. Int. J. of Engineering Science, 16: 879-903.

Kennedy RP (1976) Review of procedures for the analysis and design of concrete structures to resist missile impact effects. Nuclear Engineering and Design, 37:183-203.

Kotsovos MD and Pavlovic MN (1995) Structural Concrete, Finite Element Analysis for Limit State Design. Thomas Telford Publications: London.

Laible RC (1980) Ballistic Materials and Penetration Mechanics: Methods and Phenomena. Elsevier: Amsterdam.

Li JC (2001) Investigation of high velocity long rod penetrating semi-infinite concrete target. PhD. Thesis, Xi'an Jiaotong University, Xi'an, China (in Chinese, English abstract).

Libersky LD and Petscheck AG (1991) Smoothed particle hydrodynamics with strength of materials. Proceedings of the Next Free Lagrange Conf. Springer-Verlag: NY, pp 248-257.

Liu MB, Liu GR, Zong Z and Lam KY (2003) Computer simulation of the high explosive explosion using smoothed particle hydrodynamics methodology. Computers & Fluids, 32(3): 305-322.

Liu GR (2002) Mesh Free Methods: moving beyond the finite element method. CRC press: Boca Raton.

Lucy LB (1977) A numerical approach to the testing of the fission hypothesis. The Astronomical Journal, 82(12): 1013-1024.

Mazars J (1986) A description of micro- and macroscale damage of concrete structures. Engineering Fracture Mechanics, 25(5-6): 729-737.

Persson AKE(1990) CMl-A Simple Model for the dynamic deformation and failure properties of brittle materials. Dynamic Research AB Report: Sweden.

Qiang HF and Fan SC (2002) Numerical simulation of perforation of concrete slabs by steel rods using SPH method . The 2nd International Conference on Structural Stability and Dynamics. December 16-18, Singapore.

Riedel W, Thoma K, Hiermaier S and Schmolinske E (1999) Penetration of reinforced concrete by BETA-B-500-Numerical analysis using a new macroscopic concrete model for hydrocodes, Proceedings of 9th Int. Symp. IEMS, Berlin, pp 315-322.

Shiu WJ, Donzé FV and Daudeville L (2009) Influence of the reinforcement on penetration and perforation of concrete targets: A discrete element analysis. Engineering Computations: International Journal for Computer-Aided Engineering and Software, 26(1/2): 29-45.

Wang YB (2003) Research in Structural Impacting Problems based on Unified Strength Theory. PhD. thesis, Xi'an Jiaotong University, Xi'an, China (in Chinese, English abstract).

Wei XY (2002) Investigation of Long Rod Penetrating Target. PhD. thesis, Xi'an Jiaotong University, Xi'an, China (in Chinese, English abstract).

Yu MH, He LN and Song LY (1985) Twin shear stress theory and its generalization. Scientia Sinica (Sciences in China), English Edition, Series A, 28(11): 1174-1183.

Yu MH and He LN (1991) A new model and theory on yield and failure of materials under the complex stress state. In: Mechanical Behavior of

Materials-6, (ICM-6). Jono M and Inoue T ed., Pergamon Press: Oxford, Vol. 3, pp 841-846.
Yu MH (1992) New System for Strength Theory. Xi'an Jiaotong University Press: Xi'an, China (in Chinese).
Yu MH (1998) Twin Shear Theory and its Applications. Science Press: Beijing (in Chinese).
Yu MH (2002) Concrete Strength Theory and its Applications. Higher Education Press: Beijing (in Chinese).
Yu MH (2002) Advances in strength theories for materials under complex stress state in the 20th Century. Applied Mechanics Reviews, 55(3): 169-218.
Yu MH (2004) Unified Strength Theory and its Applications. Springer: Berlin.
Yu MH, et al (2006) Generalized Plasticity. Springer: Berlin.
Zhou XQ (2002) Numerical Analysis of Reinforcement Concrete Using Multi-Surface Strength Model. Doctoral thesis at Nanyang Technological University, Singapore.
Zhou XQ, Hao H, Li ZX (2007) Numerical simulation of an underground structure under a hypothetic terrorist bombing. Journal of PLA University of Science and Technology (Natural Science Edition), 8(6): 567-572 (in Chinese).